

Evolution of Fracture Mode in Nano-twinned Fe-1.1C-12.5Mn Steel

MAHMOUD KHEDR,^{1,2,3} LI WEI,^{1,2,5} MIN NA,⁴ LI YU,² and
JIN XUEJUN^{1,2,6}

1.—Shanghai Key Laboratory of Material Laser Processing and Modification, Shanghai Jiao Tong University, Shanghai 200240, China. 2.—State Key Laboratory of Metal Matrix Composites, School of Materials Science and Engineering, Shanghai Jiao Tong University, Shanghai 200240, China. 3.—Mechanical Department, Faculty of Engineering at Shoubra, Benha University, Cairo 11629, Egypt. 4.—Key Laboratory for Microstructures, Shanghai University, Shanghai 200444, China. 5.—e-mail: weilee@sjtu.edu.cn. 6.—e-mail: jin@sjtu.edu.cn

The evolution of fracture mode was investigated in Fe-1.1C-12.5Mn steel with prior introduced nano-twinned structures. The thicknesses of the prior twin plates were manipulated by thermo-mechanical treatments. During the plastic deformation, thin prior twin plates (30–40 nm) were penetrated by dislocations which activated secondary twin systems, and therefore dimple features were promoted in the fractured surfaces due to dislocation accommodation within the nano-twin plates. However, dislocation pile-up on the boundaries of the thick prior twin plates (90 nm) led to trans-granular fracture and formation of cracks. Moreover, prior twin elimination enhanced inter-granular feature appearance in the fractured surfaces because of dislocation accumulation on grain boundaries.

INTRODUCTION

The mechanical performance of twinning-induced plasticity (TWIP) steels is controlled by dislocation behaviors.¹ TWIP steels possess stacking fault energy (Γ) ranging between 18 mJ m⁻² and 50 mJ m⁻².^{2,3} Due to the low value of Γ , during plastic deformation of TWIP steels, dislocations dissociate into partials which activate the formation of twin plates.^{4–6} Twin boundaries are $\Sigma 3$ boundaries⁷ which work as planar obstacles where dislocations are stopped.⁸ Thus, the mean free path of dislocations (Λ) decreases with the initiation of twin plates during the plastic deformation, known as the dynamic Hall–Pitch effect.^{2,9}

A localized plastic deformation occurs in Fe-1.2C-12Mn steel because of the existence of twinned and not-twinned grains,^{10,11} which leads to premature failure of high-Mn TWIP steel due to inhomogeneous twins distribution.¹² Moreover, an enhanced dislocation movement caused by hydrogen expedites the failure of austenitic TWIP steels, which promotes inter-granular features in the fractured sur-

faces due to dislocation accumulation on the grain boundaries.^{13,14} However, promotion of dimple features in the fractured surfaces is attributed to the increase of the twin volume fraction associated with a strain rate rise.¹¹ Therefore, an obstruction of dislocations to prevent their accumulation on the grain boundaries can lead to an increased life time until failure in the ternary Fe-C-Mn steels.

Furthermore, nano-twinned structures can be introduced in face-centered cubic materials.¹⁵ The nano-twinned materials contain coherent twin boundaries (CTBs) which can be produced via electro-deposition or thermo-mechanical processing.^{14–18} Existing coherent twin plates (CTPs) protect the grain boundaries from being attacked by dislocations.⁷ In this case, the grain size is not as effective as the twin lamellae spacing which is a characteristic property in the nano-twinned structures.

In the present study, we investigate the effect of the CTP thicknesses on the obstruction of dislocation movements and consequently show the effect of dislocation evolution on changing of the fracture mode in nano-twinned ternary Fe-1.1C-12.5Mn steel.

MATERIALS AND PRODUCTION OF THE PRIOR TWINS

The steel was melted and cast into round billets of 50 kg in a vacuum. After homogenization at 1100°C for 60 min, the billets were hot-rolled in a pilot hot-rolling mill to a thickness of 12 mm with a finish temperature of 650°C, followed by water-cooling to room temperature. The hot-rolled strips were further annealed at 1000°C for 30 min followed by water-quenching, and the final microstructure is austenite with a grain size of $65 \pm 15 \mu\text{m}$.

Deformation twins were introduced to the homogenized hot-rolled plates via cold rolling with a total thickness reduction of 30% through 8 paths. The cold-rolled plates were cut into thin sheets with thicknesses of $1 \pm 0.05 \text{ mm}$. Residual strains accompanying the cold-rolling processes were reduced by holding the cold-rolled sheets at 915°C for 40 s, 90 s and 120 s followed by water-quenching (labeled as CR40, CR90 and CR120 respectively). To achieve a full recovery, the cold-rolled samples were annealed at 1000°C for 300 s followed by water-quenching (labeled as CR300). The selection of annealing temperatures at more than 900°C was designed to avoid forming carbide precipitations.^{19,20} Figure 1 exhibits the thermo-mechanical processing indicating sample codes.

EXPERIMENTAL WORK

X-ray diffraction (XRD) was carried out by a RIGAKU ULTIMAIV with a Ni filter operating at 40 kV and 30 mA using a copper tube conducted between 40° and 100° at a speed of 2° per min. XRD was performed to evaluate phase stability and dislocation density after the thermo-mechanical treatments. Dislocation density (ρ) was calculated via the MAUD software program.²¹

Dog-bone-shaped samples for tension tests were prepared according to the ASTM standard (E 8M-03) with gauge dimensions of $25 \times 6 \times 1 \text{ mm}^3$. The tension tests were performed at room temperature with a strain rate of 10^{-5} s^{-1} using a Zwick (Z100) universal testing machine. After the tension tests, fracture morphologies were observed using scanning electron microscopy (SEM) with a JEOL JSM7600F, field-emission electron microscope operated at 15 kV.

An Olympus GX-71 optical microscope was used to record the microstructure. Transmission electron microscopy (TEM) was carried out using a JEOL 2100F operated at 200 kV. TEM was performed to investigate the microstructure evolution before and after the tension tests. After tensile testing of CR40 and CR90, the specimens were examined by means of AZTEC HKL electron backscattered diffraction (EBSD) instrument in a ZEISS SUPRA55 SEM.

RESULTS AND DISCUSSION

The Microstructure Before Tension Test

Figure 2 shows the microstructure of the specimens via OM and TEM before tension tests. Although, the holding time of the cold-rolled samples during the heat treatments was different, the grain size of the specimens is nearly the same ($\sim 33 \pm 6 \mu\text{m}$). Deformation marks appearing via OM in CR40, CR90 and CR120 represent CTPs as evidenced by the TEM. Moreover, twin plate thicknesses and the surrounding dislocation tangles decrease with increasing of the annealing time from 40 s to 120 s at 915°C. At the same time, no carbides are observed in the microstructure.

The stability of the twins and dislocations is sensitive to the annealing holding time and the temperature during the heat treatments.^{15,17}

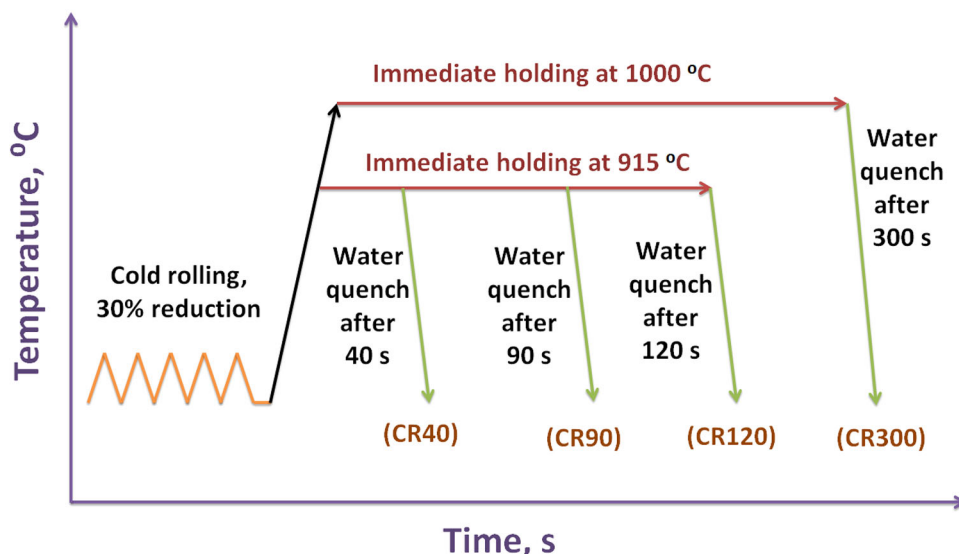


Fig. 1. Schematic drawing of the thermo-mechanical processing showing samples codes.

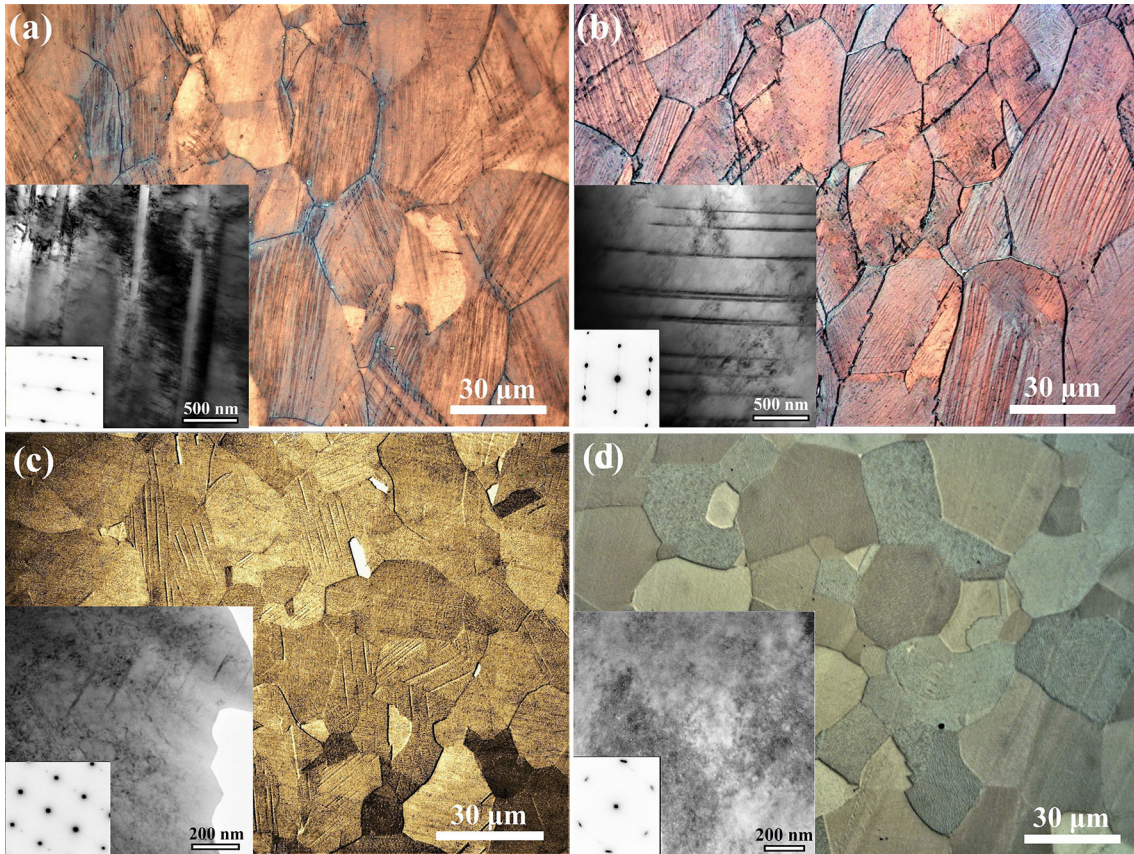


Fig. 2. Microstructure evolution after flash annealing followed by water-quenching of the nano-twinned specimens via OM and TEM (in the insets): (a) CR40, (b) CR90, (c) CR120 and (d) CR300. The insets show the diffraction patterns along the $[011]_{\gamma}$ zone axis.

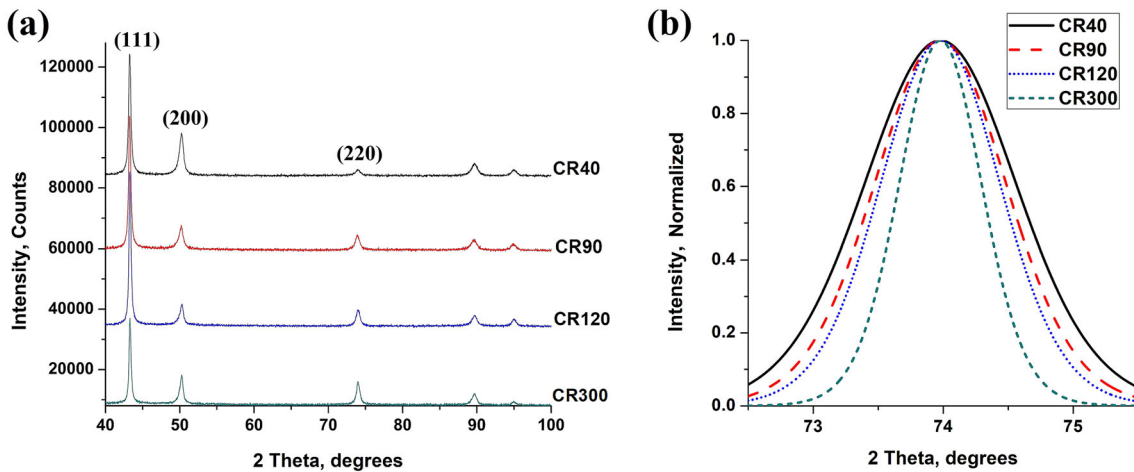


Fig. 3. (a) X-ray diffraction patterns of CR0, CR40, CR90 and CR300, (b) the corresponding Pearson VII fitting curves of (220) peaks.

Therefore, some twin planes are reoriented like the parent matrix orientation (de-twinning phenomenon) and the thicknesses of the CTPs decrease gradually with increasing of the annealing holding time.²² Furthermore, annealing of the nano-twinned specimens for 300 s at 1000°C results in the disappearance of the CTPs.

Figure 3a shows the XRD patterns of CR40, CR90, CR120 and CR300. Clearly, the current phase is only austenite. Figure 3b shows the Pearson VII fitting curves of the peak profiles diffracted at (220) of the CR40, CR90, CR120 and CR300. CR40 displays the largest peak broadening which indicates that it has dislocation densities, twin plate volume fractions and micro-strains greater than the

other specimens (CR90, CR120 and CR300). In other words, the broadening of the peak profiles can be processed to calculate the values of dislocation densities.^{23–26} In order to estimate the dislocation density, the values of the lattice constant (a), crystallite size (d) and micro-strain (ε) of the current phases were calculated by the MAUD program.²¹ The dislocation densities (ρ) can be calculated according to Eq. 1, as follows²⁶:

$$\rho = \frac{3 \times \sqrt{2\pi} \times (\varepsilon^2)^{0.5}}{d \times b} \quad (1)$$

where b is the magnitude value of Burger's vector ($b = a/(2)^{0.5}$ for the FCC structure).

The dislocation mean free path (Λ) depends on the grain size (D), the average width of the matrix lamellae existing between the twin plates (w) and the mean distance between the forest dislocations^{23–27}:

$$\frac{1}{\Lambda} = \frac{1}{D} + \frac{1}{w} + k\sqrt{\rho} \quad (2)$$

where k is a constant with a value equivalent to the strain-hardening exponent,²³ and w depends on the average width of the twinned plates (e) and twin volume fraction (F)^{25–27}:

$$\frac{1}{w} = \frac{F}{2e \times (1 - F)} \quad (3)$$

Table I shows the characteristics of the CTPs, Λ , ρ and D . An average of at least five readings are recorded in the table. The thicknesses of the CTPs were calculated based on the dark field images via TEM, while the twin volume fraction was calculated by dividing the total thicknesses of the twin plates by the total twinned area in the observed TEM images.²⁵ CR40 contains thick CTPs (90 nm), while the CR90 and CR120 show finer CTPs with thicknesses of 40 and 30 nm, respectively. On the other hand, Λ equals 150 nm in CR40, and it increases to 280 and 335 nm in CR90 and CR120, respectively. The increase of the Λ value refers to the increase of the mobile dislocation during the plastic deformation.²⁸ Moreover, ρ intensively decreases with the increase of the annealing holding time.

Tension Test Results and Fracture Mode Evolution

Figure 4a displays the tensile behaviors of the specimens. It is apparent that CR40 shows the maximum flow stress; however, it records the lowest elongation. The flow stress of the CR40 is enhanced because it possesses the lowest Λ , as well as the thickest CTPs, which require a higher external load to move the dense dislocation tangles during the plastic deformation.^{30,31}

CR90 and CR120 show the greatest values of both strength and ductility. Clearly, the increase of Λ and the decrease of CTPs thicknesses positively affect the mechanical behavior during tensile testing, which is consistent with the literature.^{15,32} However, annealing of the nano-twinned specimens for 300 s relaxes the CTPs to be re-oriented like the matrix arrangement, and the positive effect of the CTPs to hinder dislocation movements is eliminated. Therefore, the lowest strength is achieved in CR300.

Figure 4b, c, d, and e displays the fractured surfaces via SEM after tensile testing. CR40 shows a formation of tremendous cracks; however, these cracks have disappeared in the CR90 and a fully dimple structure is displayed, while limited inter-granular features appear in CR120. Moreover, CR300 (without prior twins) shows combinations of trans-/inter-granular fractures mixed with dimples.

The existence of thick CTPs prevents the mass of the dislocations cross-slipping during the plastic deformation.^{8,33} Nevertheless, in austenitic steels, the promotion of dislocation pile-up spots results in the formation of localized stress concentration zones, which initiate cracks irregularly.^{12,34} Therefore, an early fracture occurs in CR40 compared to CR90 and CR120, and the fracture surface shows the promotion of trans-granular features due to crack formation.

On the other hand, the appearance of dimple features (which is a characteristic of a ductile fracture) is attributed to the enhancing of microvoid coalescence, since dislocations serve as void nucleation sources in the fractured surfaces.¹¹ This leads us to conclude that the dislocations are being

Table I. Characteristics of the CTPs, Λ , ρ and D of the specimens before tensile testing

Sample condition	CR40	CR90	CR120	CR300
CTPs thickness (nm)	90 ± 25	40 ± 10	30 ± 5	–
CTPs volume fraction (%)	16 ± 2	12.5 ± 0.5	8 ± 1	–
Λ (nm)	150 ± 25	280 ± 10	335 ± 5	~ D
$\rho \times 10^{13}$ (m ⁻²)	40 ± 5	2.76 ± 0.6	1.1 ± 0.1	0.08 ± 0.04
D (μ m)	33 ± 6	33 ± 6	33 ± 6	33 ± 6

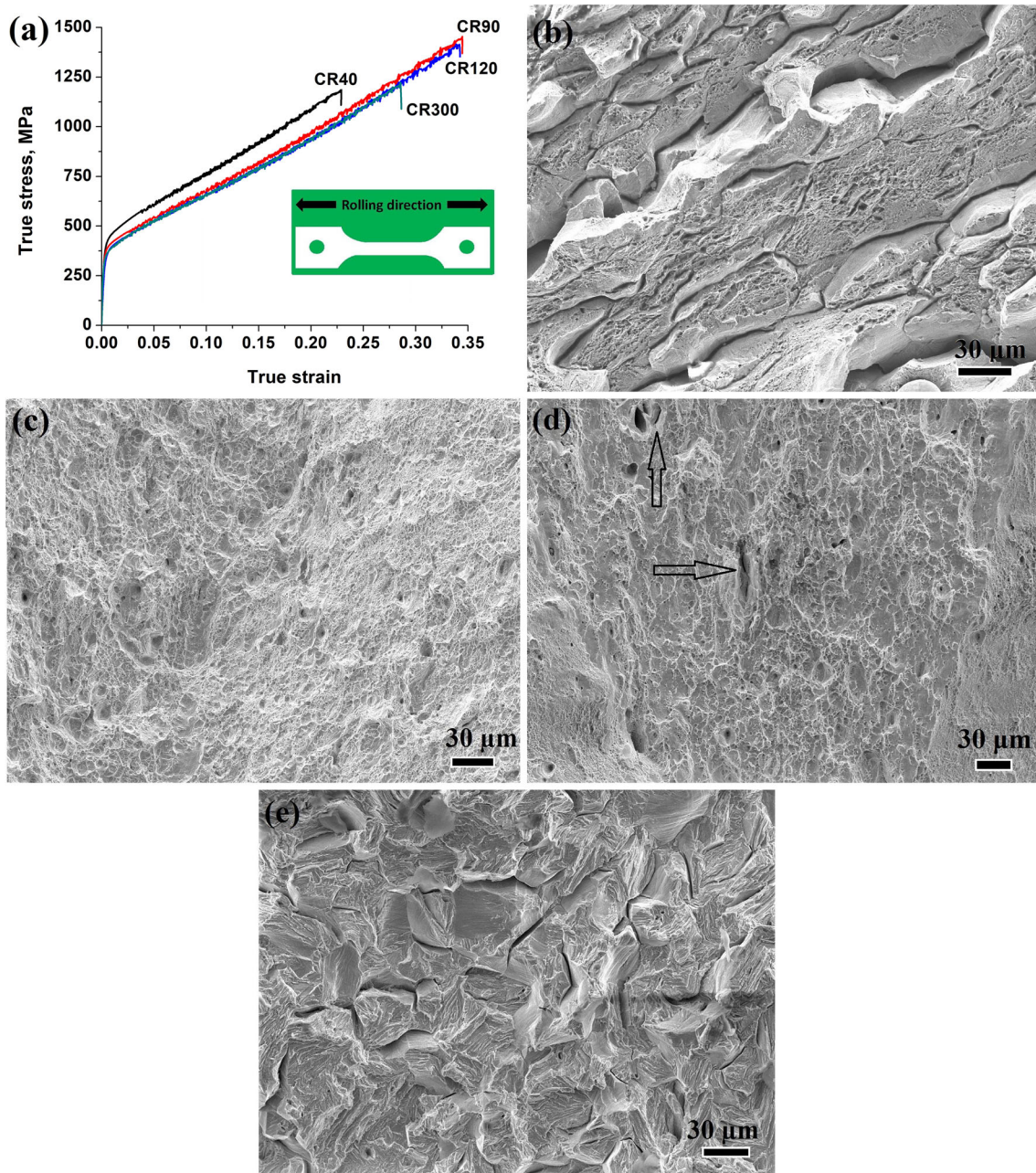


Fig. 4. (a) Stress–strain curves of the specimens. Fracture surfaces via SEM: (b) CR40, (c) CR90, (d) CR120 and (e) CR300. The arrows in (d) refer to the appearance of few inter-granular features in CR120.

homogeneously distributed through the twin/matrix in CR90 and CR120.

In ternary Fe-1.1C-12Mn steel, the inter-granular fracture appearance is attributed to dislocation accumulations on the grain boundaries.^{11,13} Dislocation cross-slipping is enhanced in CR300 because of the disappearance of CTPs. Therefore, dislocations accumulate on the grain boundaries, and inter-granular features are increased compared to the other nano-twinned specimens.

The Microstructure After Tension Test

Figure 5 shows the EBSD results of CR40 and CR90 upon fracture after tensile testing within the gauge region. Clearly, intersections of the twin plates with different orientations prevent its development in CR40. Based on the color distribution according to Kernel average misorientation (KAM), dislocations are accumulated on the twin and grain boundaries. However, in CR90, enhanced intersec-

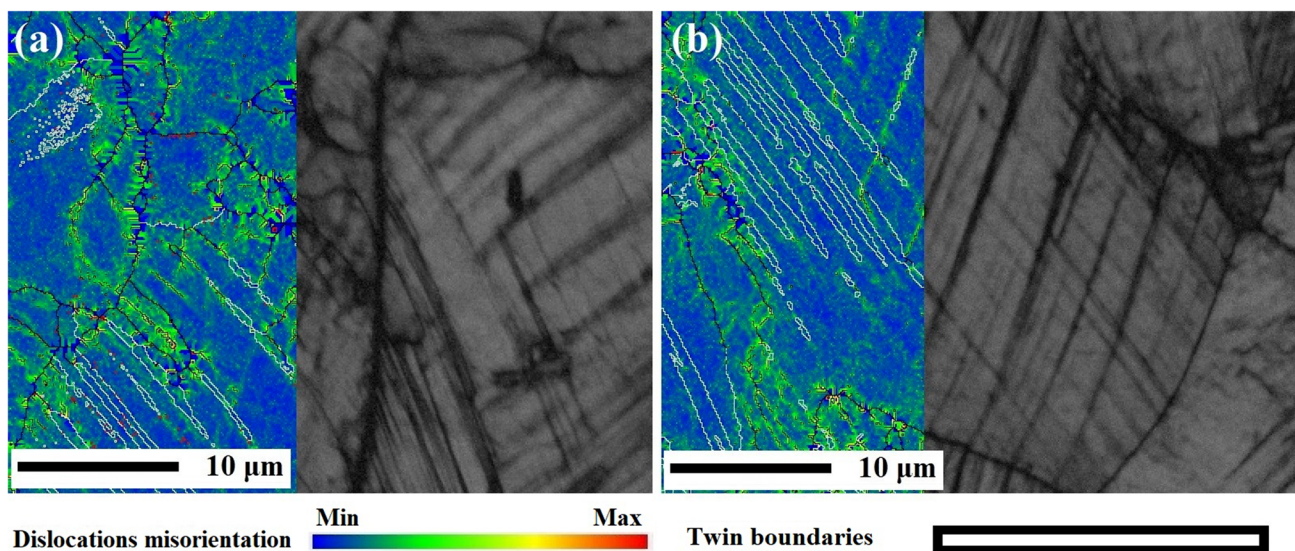


Fig. 5. EBSD images after tension tests: (a) CR40, (b) CR90 (Color figure online).

tions between the primary and secondary twins are recorded, which enhance the homogenous distribution of the internal stresses and dislocations inside the grains. According to the EBSD results, the volume fraction of the twin boundaries in CR40 is approximately 13%, while it is increased to approximately 14.3% in CR90. The volume fraction of the low-angle grain boundaries in CR40 and CR90 is 80% and 81.1%, respectively. These values refer to the enhancing of the mechanical twinning in CR90 compared to CR40.

Figure 6 presents the microstructures upon fracture after tension tests via TEM within the gauge region. Figure 6a shows the formation of very thick twin plates ($e \sim 350 \pm 70$ nm) in the CR40, as well as dislocation tangles accumulated on the boundaries of these thick plates. Figure 6b shows a well-distributed fine twin plates ($e \sim 120 \pm 50$ nm) intersect with secondary twin plates in CR90. The twin plates approximately occupy 90% of the area fraction of the TEM image. There are no arrangements of dislocation cells in the microstructure. Twin plates can be considered as dislocation reservoirs,⁴⁻⁶ and therefore dislocations are being accommodated in the mechanically induced twins. The microstructures shown in Fig. 6a and b via TEM agree with the EBSD results (as shown in Fig. 5).

Figure 6c shows intersections between primary and secondary twin plates in CR120 similar to CR90, while its volume fraction is lower than in CR90. Figure 6d exhibits a reduction of the mechanically produced twin plates in addition to the appearance of dislocation forests in CR300.

During the plastic deformation, dislocations are being accumulated in front of the CTBs followed by twin boundaries penetration.^{29,35} The initially thick CTPs hinder the dislocation passage, which

increases the local stress values there, although it will be relaxed via increasing of the twin plate thicknesses.^{36,37} Therefore, CR40 showed the formation of very thick twin plates during tensile testing, but nevertheless cracks are initiated there in paths parallel to the CTBs after reaching a saturation of fault energetics as discussed in Refs. 7, 38, and 39. When thin CTPs are being penetrated by dislocations, it can change the stacking sequence in the planes intersecting with them, as reported in Ref. 29. Therefore, secondary twin systems are promoted, and dislocations are stored through the mechanically induced twin plates instead of by random accumulations on twin and grain boundaries. Consequently, CR90 and CR120 show values of strength and ductility greater than CR40. However, the flow stresses in CR90 and CR120 are negatively affected by the softening mechanism caused by dislocations due to CTPs penetration.²⁹

In CR40, the production of thick twin plates results in a heavy dislocation accumulation on its boundaries. Therefore, premature failure occurs because of crack formation (Fig. 4b) attributed to the localized stress concentration. However, in CR90 and CR120, enhanced primary and secondary twin intersections result in dislocation accommodation through these twin plates. Moreover, the fractured surfaces showed promotion of dimple features (Fig. 4c and d). As a result, the strength and ductility are enhanced due to the homogeneous distribution of dislocations within the grains. On the other hand, in the initially twin-free specimen (CR300), dislocation cross-slipping is activated due to the absence of the planar obstacles (CTPs). Therefore, dislocations are accumulated on the grain boundaries, and inter-granular fracture is promoted (Fig. 4e).

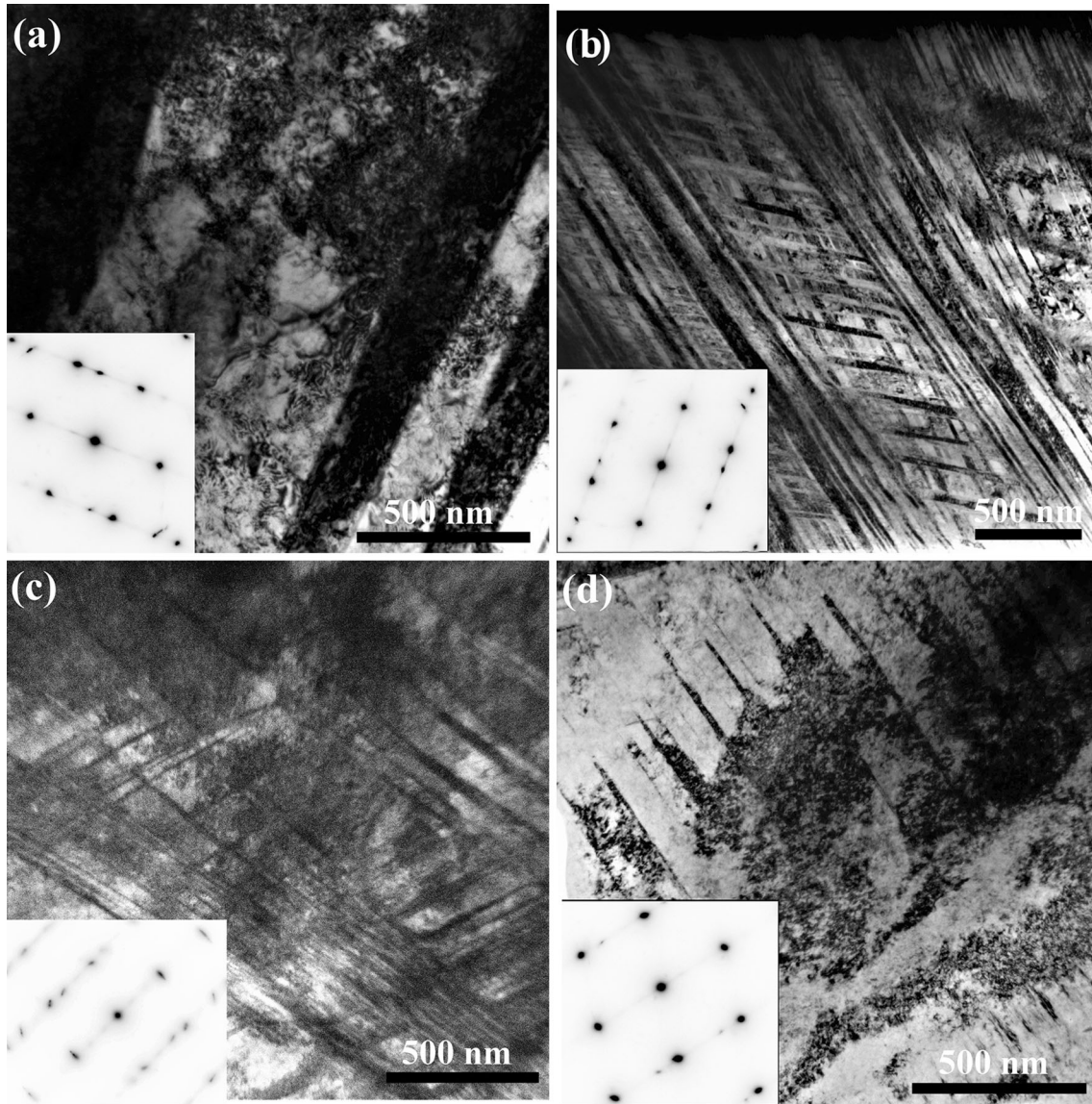


Fig. 6. Microstructure evolution after tension tests via TEM: (a) CR40, (b) CR90, (c) CR120 and (d) CR300. The insets show the diffraction patterns along the $[011]_{\gamma}$ zone axis.

Effect of the Prior Twins on the Dislocation Mean Free Path

During the plastic deformation of materials with nano-grain size, the induced shear strain (μ) produced by dislocations was proposed by Bouaziz et al.²³ It can be modified in nano-twinned materials (considering Λ to be more effective than D) as follows:

$$\mu = \frac{b}{\Lambda} \quad (4)$$

where b is the magnitude of the dislocation Burgers vector. Furthermore, dislocations take the time t_p to transfer between the twin plates, which depends on the shear strain rate μ :

$$t_p = \frac{\mu}{\mu'} \frac{b}{\Lambda \times \mu'} \quad (5)$$

In addition, the relaxation time consumed during dislocation diffusion in order to be accommodated within the boundaries is defined as t_r ²³:

$$t_r = \frac{\Lambda^2}{T_{bd}} \quad (6)$$

where T_{bd} is the twin boundary diffusion. However, with CTPs disappearance, t_p equals $b/(D\mu)$ and t_r equals D^2/G_{bd} , where G_{bd} is the grain boundary diffusion.

Based on Eqs. 5 and 6, with a reduction of Λ , the time taken by dislocations to travel between the twin plates becomes longer; however, the relaxation time consumed during dislocation diffusion to be accommodated (stored) in the boundaries becomes shorter. This behavior enhances dislocation accumulation on the twin boundaries, and cracks can be easily initiated as happens in CR40; meanwhile, the reduction of Λ improves the flow stress of the material due to the promotion of the hardening mode as reported in Ref. 29. On the other hand, with an increase of Λ , t_p is reduced and there will be enough time for dislocations to be accommodated within the matrix in-between the twin lamellae, which promotes the mechanical twinning, as happens in CR90 and CR120. However, the flow stress is negatively affected due to the promotion of the softening mode caused by dislocation movement.²⁹

Values of Λ directly influence the mechanical behavior of the nano-twinned Fe-1.1C-12.5Mn steel, and the critical value of dislocation mean free path (Λ_c) is expected to range between 280 and 335 nm, which should be further investigated. We believe that when $\Lambda > \Lambda_c$, the smaller Λ value induces a higher dislocation density under the same strain, similarly to the grain size effect proposed by Bouaziz et al.²³ Nevertheless, when $\Lambda < \Lambda_c$, a softening mechanism does not occur because the twin boundaries are not prone to absorb dislocations as easily as the grain boundaries, which needs further discussion.

MODELING OF THE FLOW STRESS

The flow stress (σ_f) in austenitic steels can be expressed as follows⁴⁰:

$$\sigma_f = \sigma_y + \sigma_t + \sigma_d \quad (7)$$

where σ_y is the yield strength, and σ_t and σ_d are the strengths contributed by mechanical twinning and dislocation storage, respectively, which can be calculated as follows^{1,5,6}:

$$\sigma_t = \frac{GM\beta b}{\Lambda} \quad (8)$$

$$\sigma_d = GM\alpha b\sqrt{\rho} \quad (9)$$

where G is the modulus of rigidity, being approximately 70 GPa, M is the Taylor factor with value 3, and β and α are constants with values of 0.3 and 0.1, respectively.^{26,27,41,42}

During the plastic deformation, the flow stress depends on the change of σ_t and σ_d with respect to the strain change ($d\varepsilon$), as follows:

$$\frac{d\sigma_f}{d\varepsilon} = \frac{d\sigma_t}{d\varepsilon} + \frac{d\sigma_d}{d\varepsilon} \quad (10)$$

The change of σ_t with respect to ε is directly related to the change of the twins' volume fraction F :

$$\frac{dF}{d\varepsilon} = (1 - F_0)NV_{tw} \quad (11)$$

where F_0 is the volume fraction of the CTPs, $(1 - F_0)$ means the initiation of the mechanical twins through the matrix, while it indicates a reduction of the twin probability with increasing the volume fraction of the CTPs, and N is the number of nuclei per unit volume which depends on the probability of a successful nucleation as follows⁴³:

$$N = N_0 \exp\left[-\left(\frac{\sigma_{crit}}{\sigma}\right)^{s1}\right] \quad (12)$$

where $s1$ is a twinning probability exponent equal to 1.4, N_0 is a scaling constant with a value 3.6×10^{18} ,⁴³ and σ_{crit} is the critical stress required to form an intrinsic stacking fault⁴⁴:

$$\sigma_{crit} = 6.14 \frac{\Gamma}{b_b} \quad (13)$$

where b_b is the magnitude of Burgers vector of a partial dislocation equal to $b/\sqrt{3}$.

Furthermore, V_{tw} is the volume of the mechanically induced twin plates, and depends on the critical mechanically induced twin plate width r^* , twin thickness t (is assumed to be 100 nm) and twin plate length l which tends to the grain size⁴²:

$$V_{tw} = r^*tl = r^*tD \quad (14)$$

The supplementary materials show a graphical representation of r^* , t and l (see supplementary Figure S1). Furthermore, during the plastic deformation, we assume that the thicknesses of the CTPs increase according to Eq. 15 as follows:

$$e = e_0 \exp(\varepsilon)^{s2} \quad (15)$$

where e_0 is the initial thickness of the CTPs after annealing, and $s2$ is a fitting parameter with a value equal to 4. The evolution of e during tensile testing in CR40, CR90 and CR120 based on Eq. 15 is compared with the experimental values upon fracture in the supplementary Figure S2. However, e is assumed to be constant with a value of 30 nm in CR300 which is CTPs free.⁴²

On the other hand, the change of σ_d is directly related to the change of ρ with respect to ε , as follows^{23,40,42,43}:

$$\frac{d\rho}{d\varepsilon} = M \left[\frac{k1}{b} \sqrt{\rho} + \frac{m_{sf}F}{\Lambda b} - f_{DR}\rho \right] \quad (16)$$

where $k1 = 0.06$ is a constant valid for austenitic steels,⁴² m_{sf} is the Schmid factor of $\langle 112 \rangle \{111\}$ stacking faults formed from $\langle 110 \rangle \{111\}$ perfect dislocations and approximately equals 0.31,⁴² and f_{DR} is the dynamic recovery factor at room temperature, taken as 3.5.⁴²

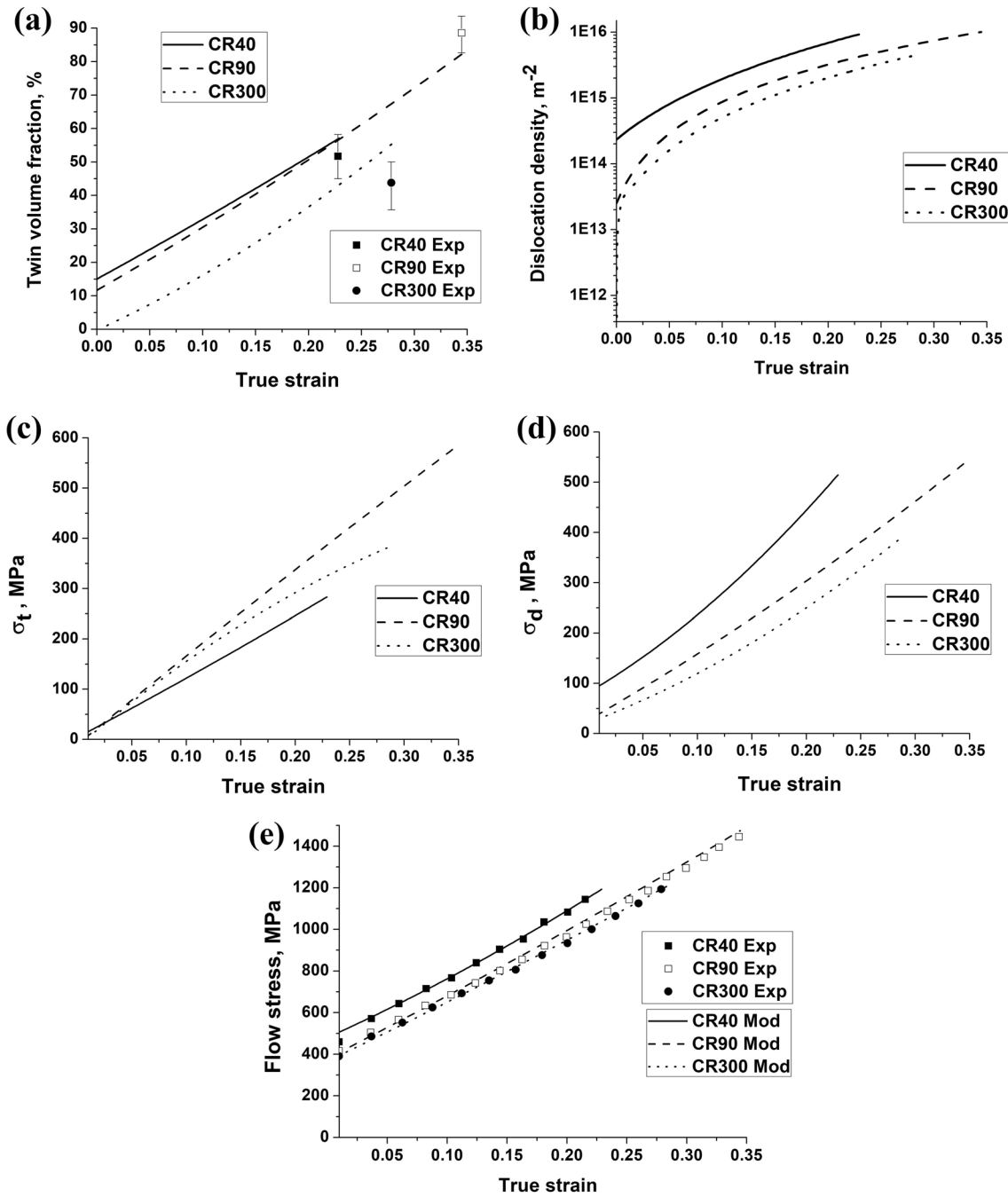


Fig. 7. Evolution of (a) twin volume fraction and (b) dislocation density during tensile testing, (c) the contribution of mechanical twinning to the flow stress, (d) the contribution of dislocation accumulation to the flow stress, (e) comparison of the experimental and modeled flow stresses in CR40, CR90 and CR300.

Figure 7a and b shows the evolution of F and ρ during tensile testing. It is apparent that CR40 shows the greatest values of F . However, the twin volume fraction increase in CR40 is attributed to the widening of twin plate thicknesses which is a twin growth event,³⁶ and it does not effectively contribute to the flow stress. Furthermore, CR40 displays the greatest dislocation density during the plastic deformation due to the initial high ρ and low value of Λ .

Figure 7c and d show the contribution of mechanical twinning and forest hardening caused by dislocation accumulation to the flow stresses of CR40, CR90 and CR300 based on Eqs. 8 and 9. Clearly, CR40 shows a flow stress contributed by twinning lower than CR90 and CR300, which is attributed to the widening of the twin plate thicknesses which is a twin growth event, and the flow stress is negatively affected.³⁶ However, the CR90 shows the maximum flow stress contributed by twinning

which confirms the promotion of the mechanical twinning. Furthermore, the flow stress contributed by dislocation accumulation is a maximum in CR40 due to the initial high dislocation density and the low value of Λ before tensile testing. Meanwhile, CR300 shows that σ_d contributed the lowest values to the flow stress due to the initial recovery of the dislocations and CTPs (because of annealing for 300 s) before the tension test.

Furthermore, CR90 achieves the maximum values of σ_t , which refers to the promotion of dimple feature formation in the fractured surfaces as a result of the homogeneous distribution of the dislocations inside the mechanically induced twin plates. However, the appearance of the trans-granular features after the fracture of CR40 is attributed to the high values of σ_d due to the tremendous values of ρ which accumulate on the boundaries of the thick twin plates, while it accelerates the occurrence of the premature failure of CR40 compared to CR90.

Figure 7e shows the flow stress as calculated by Eq. 7 compared to the experimental values during tensile testing. It exhibits good agreements between the modeling and the experiments. Dislocation accumulation enhances the flow stress in CR40, while the promotion of twinning increases the tensile strength and ductility in CR90.

SUMMARY

To conclude, nano-twinned Fe-1.1C-12.5Mn specimens with thick CTPs ($e \sim 90$ nm) and low Λ (~ 150 nm) showed premature failure during tensile testing compared to the specimens with thin CTPs (~ 30 – 40 nm) and greater Λ (~ 280 – 335 nm). This premature failure is attributed to the promotion of crack formation caused by dislocation accumulation on the CTBs with trans-granular fractures being promoted. However, the strength and ductility are enhanced in the nano-twinned specimens with thin CTPs, because the dislocations are being homogeneously distributed and stored through the mechanically induced twin plates, which causes the dimple fracture mode. Moreover, inter-granular fractures appear due to a reduced twin volume fraction and excessive accumulation of dislocations on the grain boundaries.

ACKNOWLEDGEMENTS

The authors are grateful to the financial support of the Chinese Scholarship Council (CSC), National Key R&D Program of China (No. 2017YFB0703003), National Natural Science Foundation of China (U1564203, Nos. 51571141 and 51201105), the Interdisciplinary Program of Shanghai Jiao Tong University (No. YG2014MS23), and the support sponsored by Program of Shanghai Academic Research Leader and provided by Shanghai Key Laboratory of Materials Laser Processing and Modification, Shanghai Jiao Tong University. In

addition, this research was supported by the Tescan China and Baosteel companies.

ELECTRONIC SUPPLEMENTARY MATERIAL

The online version of this article (<https://doi.org/10.1007/s11837-019-03329-7>) contains supplementary material, which is available to authorized users.

REFERENCES

1. Z.C. Luo and M.X. Huang, *Scr. Mater.* 142, 28 (2018).
2. B.C. DeCooman, Y. Estrin, and S.K. Kim, *Acta Mater.* 142, 283 (2018).
3. A. Saeed-Akbari, J. Imlau, U. Prael, and W. Bleck, *Metall. Mater. Trans. A* 40A, 3076 (2009).
4. H. Idrissi, K. Renard, L. Ryelandt, D. Schryvers, and P.J. Jacques, *Acta Mater.* 58, 2464 (2010).
5. H. Idrissi, K. Renard, D. Schryvers, and P.J. Jacques, *Scr. Mater.* 63, 961 (2010).
6. K. Renard, H. Idrissi, D. Schryvers, and P.J. Jacques, *Scr. Mater.* 66, 966 (2012).
7. P. Chowdhury, H. Sehitoglu, and R. Rateick, *Curr. Opin. Sol. Stat. Mater. Sci.* 20, 140 (2016).
8. J.R. Greer, *Nat. Mater.* 12, 689 (2013).
9. N. Hansen, *Scr. Mater.* 51, 801 (2004).
10. D. Canadinc, C. Efstathiou, and H. Sehitoglu, *Scr. Mater.* 59, 1103 (2008).
11. F.C. Liu, Z.N. Yang, C.L. Zheng, and F.C. Zhang, *Scr. Mater.* 66, 431 (2012).
12. K. Chin, C. Kang, S. Shin, S. Hong, S. Lee, H. Kim, K. Kim, and N. Kim, *Mater. Sci. Eng. A* 528A, 2922 (2011).
13. T. Michler, C.S. Marchi, J. Naumann, S. Weber, and M. Martin, *Int. J. Hydrogen Energy* 37, 16231 (2012).
14. M. Khedr, W. Li, X. Zhu, P. Zhou, S. Gao, and X. Jin, *Mater. Sci. Eng. A* 712A, 133 (2018).
15. K. Lu, L. Lu, and S. Suresh, *Science* 324, 349 (2009).
16. J. Hu, Y.N. Shi, X. Sauvage, G. Sha, and K. Lu, *Science* 355, 1292 (2017).
17. F.K. Yan, G.Z. Liu, N.R. Tao, and K. Lu, *Acta Mater.* 60, 1059 (2012).
18. L. Lu, R. Schwaiger, Z.W. Shan, M. Dao, K. Lu, and S. Suresh, *Acta Mater.* 53, 2169 (2005).
19. C. Chen, F.C. Zhang, F. Wang, H. Liu, and B.D. Yu, *Mater. Sci. Eng. A* 679A, 95 (2017).
20. A. Goldberg, O.A. Ruano, and O.D. Sherby, *Mater. Sci. Eng. A* 150A, 187 (1992).
21. L. Lutterotti, MAUD, Version 2.55 (2016). <http://www.ing.unitn.it/~luttero/maud>.
22. D. Drozdzenko, J. Bohlenb, S. Yib, P. Minárika, F. Chmelíka, and P. Dobroň, *Acta Mater.* 110, 103 (2016).
23. O. Bouaziz, Y. Estrin, Y. Brechet, and J.D. Embury, *Scr. Mater.* 63, 477 (2010).
24. J.-Y. Kim, Y. Estrin, H. Beladi, I. Timokhina, K.-G. Chin, S.-K. Kim, and B.C. DeCooman, *Metall. Mater. Trans. A* 43A, 479 (2012).
25. K. Jeong, J. Jin, Y. Jung, S. Kang, and Y. Lee, *Acta Mater.* 61, 3399 (2013).
26. G. Dini, R. Ueji, A. Najafzadeh, and S.M. Monir-Vaghefi, *Mater. Sci. Eng. A* 527A, 2759 (2010).
27. Z.Y. Liang, Y.Z. Li, and M.X. Huang, *Scr. Mater.* 112, 28 (2016).
28. O. Bouaziz and N. Guelton, *Mater. Sci. Eng. A* 319A, 246 (2001).
29. N. Lu, K. Du, L. Lu, and H.Q. Ye, *Nat. Commun.* 6, 7648 (2015).
30. J. Jin and Y. Lee, *Acta Mater.* 60, 1680 (2012).

31. E.G. Astafurova, M.S. Tukeeva, G.G. Maier, E.V. Melnikov, and H.J. Maier, *Mater. Sci. Eng. A* 604A, 166 (2014).
32. L. Zhu, C. Wen, C. Gao, X. Guo, and J. Lu, *Scr. Mater.* 133, 49 (2017).
33. F. Hamdi and S. Asgari, *Metal. Mater. Trans. A* 39A, 294 (2008).
34. Y.F. Shen, L. Lu, Q.H. Lu, Z.H. Jin, and K. Lu, *Scr. Mater.* 52, 989 (2005).
35. J. Kachera, P. Eftink, B. Cui, and I.M. Robertson, *Cur. Opin. Sol. Stat. Mater. Sci.* 17, 227 (2014).
36. S. Kibey, J.B. Liu, D.D. Johnson, and H. Sehitoglu, *Acta Mater.* 55, 6843 (2007).
37. I.S. Nikulin, N.V. Kamyshanchenko, T.B. Nikulicheva, M.V. Mishunin, and K.A. Vokhmyanina, *Mater. Lett.* 182, 253 (2016).
38. A. Singh, L. Tang, M. Dao, L. Lu, and S. Suresh, *Acta Mater.* 59, 2437 (2011).
39. Z.J. Wang, Q.J. Li, Y. Li, L.C. Huang, L. Lu, M. Dao, J. Li, E. Ma, S. Suresh, and Z.W. Shan, *Nat. Commun.* 8, 1108 (2017).
40. M.I. Latypov, S. Shin, B.C. De Cooman, and H. SeopKim, *Acta Mater.* 108, 219 (2016).
41. Z.Y. Liang, W. Huang, and M.X. Huang, *Mater. Sci. Eng. A* 628A, 84 (2015).
42. E.I. Galindo-Nava and P.E.J. Rivera-Díaz-del-Castillo, *Acta Mater.* 128, 120 (2017).
43. Z.Y. Liang, X. Wang, W. Huang, and M.X. Huang, *Acta Mater.* 88, 170 (2015).
44. T.S. Byun, *Acta Mater.* 51, 3063 (2003).